ROYAL SOCIETY
OF CHEMISTRY

PAPER

Check for updates

Design, synthesis, and structural characterization of Fe²⁺-doped anatase TiO₂ nanocrystals and its impact on electronic properties and photocatalytic activity

Rayhan Hossain, [ID] *[ab] Jessica Hollow,[ab] Violet Chesterfield,[ab] Daisy Langley[ab] and Allen Apblett*[ab]

Anatase-phase TiO₂ nanorods with diameters of approximately 3 ± 1 nm and lengths of 40 ± 10 nm were successfully synthesized using a solvothermal method, followed by metal doping through thermal diffusion of Fe²⁺ ions onto the nanocrystals. The dopant incorporation process led to a significant enhancement in the visible light absorption of TiO₂, as observed from the red-shift in the UV-visible absorption spectra. This modification suggests a narrowing of the bandgap, making the material more suitable for photocatalytic applications under visible light. Specifically, Fe-doped TiO₂ nanorods with 1.0% Fe²⁺ exhibited a 35% increase in photocatalytic hydrogen production under visible light illumination compared to pure TiO₂. Electron microscopy and X-ray diffraction (XRD) analysis confirmed that the size and morphology of the nanocrystals remained unaffected by the doping process, retaining their anatase phase with no significant structural alteration. Additionally, UV-visible spectroscopy demonstrated a reduction in the bandgap energy of the TiO₂ nanorods from 3.5 eV in pure TiO₂ to a range of 3.14–3.34 eV for the Fe-doped samples. This decrease in bandgap energy is attributed to the introduction of iron ions into the TiO₂ lattice, which facilitates enhanced light absorption and improved photocatalytic efficiency. The ability to precisely control the dopant concentration while preserving the structural integrity of the TiO₂ nanocrystals is a key advantage of this method. The findings suggest that Fe-doped TiO₂ nanorods, with their enhanced photocatalytic activity, could serve as efficient materials for various applications, including hydrogen production, solar cells, and environmental sensing. These findings highlight the potential of Fe-doped TiO₂ nanorods as efficient materials for a range of clean energy technologies and environmental remediation processes.

1. Introduction

Titanium dioxide (TiO₂) remains one of the most extensively studied and widely employed materials due to its remarkable properties, including photocatalytic activity, stability, and biocompatibility. Its applications span a wide range of fields, such as environmental remediation, energy conversion, sensors, and self-cleaning surfaces.[1–9] TiO₂, particularly in its anatase polymorph, is a direct bandgap semiconductor with a bandgap of approximately 3.2 eV, which limits its optical absorption to the ultraviolet (UV) region of the electromagnetic spectrum. Given that UV light constitutes only about 5% of the solar spectrum,

this narrow absorption range significantly hampers the practical use of TiO₂ in solar-driven processes, including photocatalysis and water splitting for hydrogen production.[10–14]

To address this limitation and broaden its photoactive spectrum into the visible light range, various strategies have been explored, including doping TiO₂ with transition metals, non-metals, and incorporating nano-structural modifications. Among these approaches, doping with transition metals, particularly iron (Fe), has garnered substantial interest. Transition metal doping introduces discrete energy states within the TiO₂ bandgap, thereby lowering the material's bandgap and facilitating the absorption of photons with lower energy, thereby enabling TiO₂ to be activated by visible light. This bandgap modulation not only enhances the photocatalytic efficiency of TiO₂ under solar irradiation but also opens up new avenues for its application in environmental remediation, sustainable energy production, and antimicrobial treatments. The incorporation of iron (Fe) and other transition metals has demonstrated significant improvements in TiO₂'s

ª Department of Natural Sciences, University of Michigan, 107 Science Faculty Center, Dearborn, MI 48128, USA. E-mail: rhossain@umich.edu, allen.apblett@okstate.edu

ᵇ Department of Chemistry, Oklahoma State University, 317 Physical Science, Stillwater, OK 74078, USA

photocatalytic performance, thereby expanding its potential for real-world applications in energy conversion and environmental purification under natural sunlight.[15,16]

Iron, being a first-row transition metal, has shown promise in tuning the electronic properties of TiO_2. The successful incorporation of Fe into the TiO_2 lattice modifies its electronic structure and can either enhance or inhibit the photocatalytic activity, depending on the oxidation state and doping concentration. Iron can exist in multiple oxidation states, including Fe^{2+} and Fe^{3+}, with the most common form in TiO_2 doping being Fe^{2+}. Fe^{2+} ions substitute for Ti^{4+} in the lattice, generating defect states within the bandgap, facilitating the absorption of visible light.[17]

Furthermore, Fe doping also affects the surface properties and the ability of TiO_2 to generate reactive oxygen species (ROS), which are key to its photocatalytic activity. Iron-doped TiO_2 materials have shown improvements in the degradation of pollutants such as dyes, pesticides, and pharmaceuticals under visible light irradiation, a property that is invaluable for photocatalytic wastewater treatment.[18–23] Additionally, Fe-doped TiO_2 exhibits enhanced charge carrier separation and reduced recombination rates, which are crucial for improving the efficiency of photocatalytic reactions.[24,25]

Despite these advantages, the synthesis of Fe-doped TiO_2 nanomaterials is highly sensitive to doping concentration, annealing conditions, and the method of preparation. Excessive doping can lead to the formation of undesirable phases, such as Fe_2O_3, which may reduce the photocatalytic activity. Therefore, achieving an optimal doping concentration is crucial to maximizing the photocatalytic performance of TiO_2 while maintaining its stability.[26]

In addition to photocatalysis, Fe-doped TiO_2 has been explored for other applications, such as solar cells, sensors, and magnetic materials. Due to the magnetic properties introduced by Fe, Fe-doped TiO_2 also exhibits the potential for use in magnetic photocatalysis, where the material can be easily separated from the reaction medium, improving its reusability and cost-effectiveness. The combination of iron with titanium dioxide, especially in the form of nanocrystals, provides unique opportunities for the development of advanced materials that are both efficient and versatile. As such, Fe-doped TiO_2 nanocrystals continue to be a subject of extensive research in the fields of material science and environmental engineering.[27,28]

Transition metal doping in TiO_2 leads to the introduction of new energy levels in the bandgap. These energy levels can either serve as electron traps or act as intermediates for the transfer of charge carriers. Iron (Fe) has several oxidation states, with Fe^{2+} and Fe^{3+} being the most common in TiO_2 doping. Fe^{2+} is typically incorporated into the TiO_2 lattice, substituting for Ti^{4+}, while Fe^{3+} may exist as an impurity or interact with oxygen vacancies within the TiO_2 matrix.[29]

The introduction of Fe^{2+} into the TiO_2 lattice creates defect states that are located below the conduction band. These defect states facilitate electron excitation under visible light, allowing TiO_2 to absorb light in the visible spectrum rather than just the UV region.[30] Additionally, Fe^{2+} doping can generate oxygen vacancies and enhance the mobility of photogenerated charge carriers, leading to improved photocatalytic activity. Fe^{3+}, on the other hand, can act as an electron trap, increasing the separation of charge carriers and further enhancing the photocatalytic efficiency of Fe-doped TiO_2 under visible light.[31,32]

Fe-doped TiO_2 also benefits from the creation of oxygen vacancies, which are critical for improving photocatalytic performance. These vacancies act as active sites for photocatalytic reactions, improving the material's ability to degrade pollutants. However, excessive doping of Fe can lead to the formation of recombination centers, where the photogenerated electrons and holes recombine, reducing the overall photocatalytic efficiency. Therefore, the optimal doping concentration of Fe is crucial for maximizing the performance of TiO_2.[33]

The physical and chemical properties of Fe-doped TiO_2 are significantly altered compared to pure TiO_2, influencing its photocatalytic performance and other functional characteristics. Doping TiO_2 with Fe reduces the bandgap, shifting the absorption edge from the UV to the visible light region, typically between 2.4 and 2.8 eV. This reduction in bandgap enhances the material's ability to absorb visible light and, consequently, improves its photocatalytic activity under visible light irradiation. Additionally, the incorporation of Fe into the TiO_2 lattice causes local distortion due to the difference in ionic radii between Ti^{4+} (0.605 Å) and Fe^{2+} (0.769 Å), leading to the formation of oxygen vacancies.[34] These structural defects are essential for improving photocatalytic activity, as they provide additional active sites for reactions and enhance charge separation.

Fe-doped TiO_2 nanocrystals have shown significantly improved photocatalytic performance compared to pure TiO_2, particularly in the degradation of organic pollutants and dyes under visible light. This improvement is due to the reduced bandgap, the presence of defect states, and the enhanced charge carrier separation, which minimizes electron–hole recombination. Furthermore, at low doping concentrations, Fe-doped TiO_2 can exhibit weak magnetic properties. This feature is valuable for applications that require magnetic separability, such as in photocatalytic water treatment, where the catalyst can be easily recovered and reused. Lastly, the creation of oxygen vacancies and defect states through Fe doping improves photocatalytic efficiency by promoting electron–hole pair generation and reducing recombination. These defects also enhance the material's ability to participate in redox reactions during photocatalysis.[35]

The synthesis of Fe-doped TiO_2 nanocrystals involves various methods that determine the morphology, crystal structure, and doping concentration of the final product. The sol–gel method is a widely used and cost-effective technique for synthesizing Fe-doped TiO_2 nanocrystals. This method offers precise control over the doping concentration and particle size by adjusting the reaction conditions. The sol–gel process involves the hydrolysis and condensation of titanium alkoxides, followed by doping with iron salts. Hydrothermal and solvothermal methods involve the use of high temperature and pressure to synthesize TiO_2 nanoparticles.[36,37] These techniques result in highly crystalline TiO_2 with controlled particle sizes and doping levels. The solvothermal method allows for greater flexibility in terms of solvent choice, which can influence the crystallinity and morphology of the nanocrystals.

Co-precipitation is a widely employed method for doping titanium dioxide (TiO_2) with transition metals, including iron. This technique involves the precipitation of TiO_2 from an aqueous solution in the presence of an iron precursor, followed by thermal treatment to crystallize the TiO_2 structure. The co-precipitation method is advantageous due to its simplicity and scalability, rendering it suitable for large-scale production of Fe-doped TiO_2. However, for more precise control over doping levels, chemical vapor deposition (CVD) is an alternative approach, though less commonly employed due to its inherent complexity and high cost. CVD involves the deposition of titanium and iron precursors onto a heated substrate, facilitating fine control over doping concentrations and the formation of films with uniform characteristics. Despite these advantages, the method is generally less favored for large-scale synthesis owing to its technical demands and economic constraints. Additionally, ion implantation offers a physical doping strategy that allows for highly controlled depth and concentration profiles. In this technique, Fe ions are accelerated and implanted into the TiO_2 surface, resulting in a shallow doping profile. Ion implantation is particularly beneficial for specialized applications requiring highly tailored doping characteristics, though its application is often restricted to advanced research settings.[38–40]

TiO_2-based photocatalysts have long been studied for their potential in environmental remediation, but they face inherent limitations, such as low photocatalytic activity under visible light and rapid charge carrier recombination. To address these challenges, doping TiO_2 with transition metals like Fe(II) has gained attention, as it can introduce semi-Fenton-like properties that enhance photocatalytic efficiency. However, this process critically depends on solution pH, and traditional Fenton processes often suffer from issues like the need for acidic conditions and the degradation of catalysts over time due to the generation of reactive oxygen species. Recent studies on photocatalysts such as Z-scheme silver iodide/tungstate binary nano photocatalysts and FeO–clinoptilolite nanoparticles have highlighted alternative approaches to improve photocatalytic activity.[41,42] In our work, we design Fe(II)-doped TiO_2 nanorods, which not only improve photocatalytic activity under visible light but also mitigate the pH-dependent drawbacks of the semi-Fenton process, offering enhanced stability and efficiency across a broader pH range.

Incorporating the effects of anion vacancies, particularly sulfur, nitrogen, carbon, halogen, and oxygen vacancies, has been extensively explored in the context of photocatalysis and water splitting. Numerous recent reviews, including those focusing on the boosted effects of these vacancies in photocatalytic degradation and photoelectrochemical processes, have demonstrated their significant role in enhancing photocatalytic efficiency. The introduction of vacancies, such as oxygen vacancies, can significantly alter the electronic structure, increase charge carrier separation, and improve the reactivity of the photocatalyst. For instance, vacancies in g-C_3N_4, especially carbon and nitrogen vacancies, have been shown to enhance photocatalytic solar water splitting, providing insights into how tailored defects can optimize the material's performance.[43–46]

The novelty of the present work lies in the development of a precise and methodical two-step process for doping anatase-phase, rod-shaped TiO_2 nanocrystals with iron, which integrates surface metalation followed by thermal diffusion. This approach distinguishes itself from conventional doping techniques by offering unparalleled control over the dopant concentration. In contrast to existing methods that may lack such precision, this study innovatively combines the loading of metal ions onto the surface of TiO_2 nanocrystals with a subsequent thermal diffusion step. This method ensures the controlled incorporation of Fe^{2+} ions into the TiO_2 nanorods without altering their size, morphology, or crystalline structure, as evidenced by electron microscopy and powder X-ray diffraction analyses. The precise doping achieved through this process addresses a significant gap in the preparation of doped TiO_2 materials, enabling tailored manipulation of visible light absorption properties and facilitating enhanced photocatalytic performance.[47,48] The proposed methodology offers a robust platform for advancing TiO_2-based photocatalytic applications and other domains by harnessing the enhanced material properties afforded through meticulous doping.[49–53] This innovation represents a significant advancement in the field of materials science, providing new avenues for the development of high-performance TiO_2-based systems.

2. Materials and methods

2.1. Materials

Titanium(IV) tetraisopropoxide (TTIP, 98%), oleic acid (97%), 1-octadecene (ODE, 90% technical grade), oleylamine (OLAM), and iron(II) chloride hexahydrate were obtained from Acros Organics and TCI America. Solvents including ethanol, isopropanol, hexane, and toluene were sourced from Fisher Scientific. All reagents utilized in this study were of analytical grade and were employed without further purification. Additionally, 8-hydroxyquinoline (8-HQ) and trioctylphosphine oxide (TOPO) were procured from Acros Organics and Eastman Organic Chemicals, respectively. To maintain their stability, ODE, OLAM, and oleic acid were stored at −15 °C. All synthetic procedures were conducted under an inert nitrogen atmosphere, utilizing the Schlenk line technique to ensure an oxygen-free environment throughout the reactions. All the reactions were held in an inert N_2 atmosphere using the Schlenk line technique.

2.2. Synthesis of TiO_2 nanorods

The oleic acid-stabilized anatase-phase rod-shaped TiO_2 nanocrystals were synthesized via a non-hydrolytic ester elimination reaction, following the method developed by Hyeon et al.[32] In a typical synthesis, degassed oleic acid and titanium(IV) tetraisopropoxide were mixed and heated under an inert atmosphere at 270 °C for 2 hours. During the reflux process, volatile isopropanol was continuously vented from the reaction vessel until no further refluxing was observed at lower temperatures. Upon completion of the reaction, the mixture was cooled, and isopropanol was added to facilitate precipitation. The product was subsequently isolated by centrifugation at 3500 rpm for

8 minutes, with the supernatant discarded. The resultant precipitate was re-dispersed in hexanes to ensure uniform suspension. One sample was randomly selected for calcination to determine the mass of the produced nanorods in each sample vial, providing further insight into the yield and structural integrity of the synthesized TiO_2 nanocrystals.

2.3. Synthesis of $Fe^{2+}_{(surface)}$–TiO_2 nanorods

Fe^{2+}-surface TiO_2 nanorods with varying iron ion loadings were synthesized by surface metalation. A stoichiometric amount of the metal precursor, Fe^{2+}, in the form of oleic acid ester (ODE), was combined with oleylamine (OLAM) in a 10 : 1 mole ratio and placed in a 100 mL three-necked flask under an inert nitrogen atmosphere. The reaction mixture was subjected to vacuum at 110 °C for 1 hour to remove residual moisture and volatile components. Following this, the system was gradually heated to 250 °C at a rate of 10 °C min^{-1}, maintaining this temperature for 3 hours under nitrogen. At approximately 90 °C, a visible color change to brown indicated the formation of the iron doped TiO_2 nanocrystals. The product was precipitated by the addition of 15 mL of isopropanol, followed by centrifugation at 3500 rpm for 8 minutes. The resulting precipitate was then re-dispersed in hexane, yielding a transparent brown dispersion. To ensure the removal of any unbound iron ions, the product was precipitated and re-dispersed in hexane approximately four times. This washing procedure effectively purified the nanorods, ensuring that only the iron ions bound to the TiO_2 surface remained.

2.4. Synthesis of $Fe_{(doped)}^{2+}$–TiO_2 nanorods

Fe-doped TiO_2 nanorods were synthesized *via* thermal diffusion of surface metal ions. In this process, 8 mL of 1-octadecene (ODE) was placed in a 3-necked flask and combined with 4 mmol of Fe^{2+}-surface-loaded TiO_2 nanorods. The mixture was subjected to vacuum at 110 °C for 1 hour to remove volatiles and hexanes. After cooling to room temperature, the flask was purged with nitrogen gas to create an inert atmosphere. Subsequently, a 12 mL ODE solution containing 1 g of trioctylphosphine oxide (TOPO) was added under the nitrogen atmosphere. The reaction mixture was then heated to 250 °C and maintained for approximately 14 hours to allow for the ionic diffusion of surface metal ions into the TiO_2 nanorods. Following the reaction, 5 mL of toluene was introduced to quench the reaction. The product was precipitated by adding isopropanol, and the resulting brown precipitate was separated *via* centrifugation at 3500 rpm for 8 minutes. The precipitate was then re-dispersed in hexane, yielding a transparent brown dispersion. To remove any residual insoluble materials, the dispersion was centrifuged again at 3500 rpm for 8 minutes. Finally, the product was calcined at 450 °C for 6 hours to determine the mass of the prepared nanorods.

The synthesis yielded samples of Fe-doped TiO_2 nanorods with varying iron contents, including 1.5 mol%, 3.0 mol%, and 5.0 mol%, which contain both surface-bound and doped iron ions. The following section details the protocol to selectively remove the surface iron ions, leaving behind only the doped iron within the TiO_2 matrix, thereby isolating the doped nanocrystals for further characterization and application.

2.5. Removal of surface Fe(ɪɪ) using tris(2-aminoethyl)amine, and ethylenediamine

A centrifuge tube was charged with 1 mmol of iron-doped TiO_2 nanorods. To this, 10 equivalents of tris(2-aminoethyl)amine and ethylenediamine (L : Fe = 10 : 1) were added separately as ligands. The mixture was sonicated at room temperature for 15–25 minutes, followed by precipitation with ethanol. The resulting suspension was centrifuged at 11 000 rpm for 5 minutes, yielding a sticky brown precipitate and a colorless supernatant. The supernatant was retained, and additional ethanol was introduced to induce flocculation; however, no flocculation occurred in the supernatant. The brown precipitate was identified as iron-doped TiO_2 nanorods. Upon re-dispersion of the precipitate, a cloudy suspension was observed, which transitioned to a transparent solution upon the addition of a single drop of oleic acid. The sample was subjected to a precipitation/re-dispersion cycle three times using ethanol and hexanes and was then employed for subsequent characterization. The mass of the synthesized Fe-doped TiO_2 sample was determined by calcining a portion of the dispersion (1 mL) at 450 °C for 6 hours, and calculating the residual mass.

2.6. Photocatalytic water reduction

A 200 mL quartz flask equipped with a magnetic stirrer was charged with 10 mL of water, 2 mL of methanol, and 0.1444 g of Fe-doped TiO_2. The flask was then sealed airtight and purged with argon gas for approximately 30 minutes. Following this, a 1 mL aliquot was withdrawn from the headspace of the photocatalytic reactor and injected into a gas chromatograph (GC) to verify the absence of other gases. Subsequently, a 1 mL sample was taken at $t = 0$ to assess the gas content, and the reactor was irradiated with an unfiltered 200 W Xe Arc lamp. At predetermined time intervals, the headspace was sampled using a 1 mL gas-tight syringe, and the collected gas was analyzed *via* GC to quantify the amount of hydrogen gas evolved during the photocatalytic reaction.

2.7. Characterizations

The synthesized nanorods were characterized using a range of advanced techniques, including powder X-ray diffraction (PXRD), transmission electron microscopy (TEM), scanning electron microscopy (SEM), X-ray photoelectron spectrometer (XPS), energy dispersive X-ray spectroscopy (EDS), photoluminescence spectroscopy, and UV-visible spectroscopy. PXRD analysis was performed at room temperature using a Rigaku Ultima IV diffractometer with Cu Kα radiation (λ = 1.5408 Å) to identify the crystal phase of the nanocrystals. Diffraction data were collected over a 2θ range of 10°–80° with a step size of 0.02°. X-ray photoelectron spectroscopy (XPS) was performed using a Thermo Scientific K-Alpha X-ray photoelectron spectrometer with a monochromatized Al Kα X-ray source (1487 V). TEM imaging was conducted using a Tecnai Spirit G^2 Twin (FEI Company) instrument, equipped with a LaB$_6$ filament, operating at 120 kV. EDS analysis was employed to estimate the elemental composition of the samples. Electron micrographs were obtained using a Zeiss Sigma HD scanning electron microscope, coupled with an Oxford AZtec EDS detector, a back-scattered electron (BSE) detector, and 34° and 90° secondary-electron (SE)

detectors. UV-visible absorbance spectra were recorded using a Varian Cary 100-Bio spectrophotometer in the wavelength range of 200–800 nm. Absorption data were collected after dispersing TiO_2, Fe^{2+}-surface TiO_2, and all iron-doped TiO_2 samples in hexane and loading them into quartz cuvettes. Photoluminescence (PL) spectra were obtained with a Horiba Fluoromax-4 spectrofluorometer, utilizing a 350 W xenon lamp as the excitation source.

3. Results and discussion

3.1. Transmission electron microscopy

A representative TEM image of TiO_2 and Fe^{2+}-doped TiO_2 nanorods, post-purification, is presented in Fig. 1. The diameters
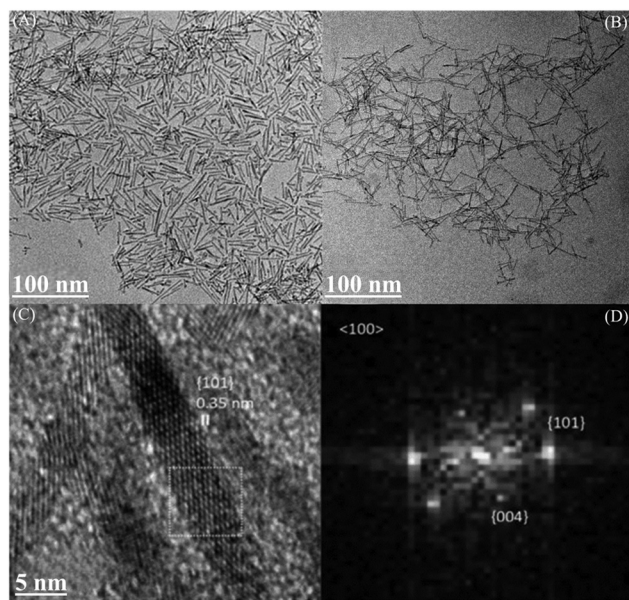

Fig. 1 TEM images of (A) synthesized TiO_2 and of (B) 3% $Fe_{(doped)}^{2+}$–TiO_2 nanorods. The scale bar is 100 nm (top left and right). (C) High-resolution TEM image of anatase TiO_2 nanorods with a scale bar of 5 nm. (D) The high-resolution image of the boxed region is shown by fast Fourier transform (FFT).

derived from TEM analysis are in good agreement with those obtained from PXRD, with a measured value of (3 ± 1) nm. These observations confirm that the Fe-doped TiO_2 nanorods are crystalline, well-dispersed, and exhibit a rod-like morphology.

At higher magnification, as depicted in Fig. 1, clear lattice fringes with a spacing of 0.35 nm were observed, corresponding to the {101} lattice planes (d-spacing = 0.351 nm; JCPDS file 21-1272). The nanocrystals, when viewed along the [100] zone axis, reveal the intersection of lattice fringes from the (011) and (01−1) planes, meeting at an angle of 43°, consistent with theoretical predictions. Additionally, less pronounced lattice fringes associated with the (004) planes were also discernible through fast Fourier transform (FFT) analysis, further confirming the crystalline nature of the nanorods.

3.2. Powder X-ray diffraction (PXRD)

The powder X-ray diffraction (PXRD) pattern (intensity *versus* 2θ) provides valuable insights into the crystallographic properties of the synthesized materials. High-intensity peaks indicate crystal planes with greater periodicity, suggesting a preferred crystal orientation, while lower-intensity peaks are indicative of more disordered or randomly oriented crystals. Notably, the pronounced peak observed at 38.7° (2θ), corresponding to the (004) reflection plane, signifies the elongation of the nanocrystals along the c-axis, characterized by a high relative intensity and narrow line width.

The phase purity and crystallinity of both pure and doped TiO_2 samples were evaluated using PXRD analysis, as illustrated in Fig. 2. The PXRD patterns of both pure and Fe-doped TiO_2 consistently show the presence of the anatase phase, with no detectable peaks corresponding to additional phases associated with metal or metal oxide impurities. This confirms the retention of the anatase crystal structure. The peak at 25.3° (2θ), associated with the (101) plane of anatase-phase TiO_2, further corroborates the phase identity, with observed values matching the standard reference (JCPDS file 21-1272).

After collection of PXRD data, structural refinements were performed using the Rietveld method. The analysis of the PXRD
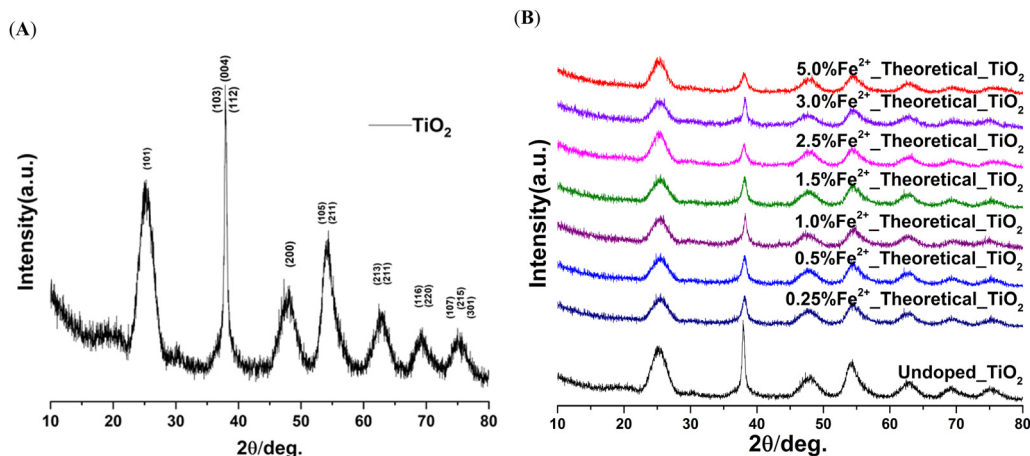

Fig. 2 XRD pattern of (A) TiO_2 nanorods and (B) $Fe_{(doped)}^{2+}$–TiO_2 samples with different dopant concentrations. The labels indicate the theoretical ratio of Fe : TiO_2 in the preparation of $Fe^{2+}_{(surface)}$–TiO_2.

Table 1 PXRD data analysis of TiO_2 nanorods and iron doped TiO_2 nanorods

Sample	Crystallinity	Crystallite size (Å)[a] (Scherrer)	Crystallite Size (Å)[a] (W–H)	Anatase d_{101}	Anatase d_{101} FWHM	Anatase d_{004}	Anatase d_{004} FWHM	Lattice parameter $a = b$ (Å)[b]	Lattice parameter c (Å)[b]	Unit cell volume (Å)³
Undoped_TiO_2	98	27.87	27.90	3.538	2.76	2.481	0.44	3.734	9.467	139.4
0.25% Fe_dTiO_2	100	32.49	32.34	3.529	2.56	2.371	0.56	3.649	9.544	138.9
0.5% Fe_dTiO_2	100	32.41	32.10	3.521	2.53	2.369	0.89	3.834	9.472	137.4
1.0% Fe_dTiO_2	98	32.12	31.98	3.516	2.69	2.359	0.74	3.894	9.646	138.4
1.5% Fe_dTiO_2	99	31.42	31.35	3.512	2.59	2.344	0.64	3.414	9.498	137.7
2.5% Fe_dTiO_2	100	33.69	32.20	3.509	2.68	2.336	0.45	3.810	9.483	136.9
3.0% Fe_dTiO_2	98	32.29	32.15	3.507	2.48	2.324	0.49	3.829	9.474	138.9
5.0% Fe_dTiO_2	99	32.94	32.60	3.504	2.67	2.314	0.94	3.624	9.464	140.4

data was carried out employing the whole pattern powder fitting (WPPF) feature of the Rigaku PDXL software. The refined structural parameters for both TiO_2 nanorods and iron doped TiO_2 nanorods are presented in Table 1. These data provide detailed insights into the crystallographic characteristics and structural integrity of the synthesized materials.

In addition to the Rietveld refinement, we also estimated the crystallite size of the final catalyst using two common methods: the Scherrer equation and the Williamson–Hall (W–H) model. Both models provide complementary information, allowing us to evaluate the effects of size and strain on the crystallites. The comparison of crystallite sizes derived from both models reveals that while the Scherrer equation provides an estimate of the size assuming no strain effects, the W–H model accounts for strain, which can significantly affect the peak broadening, especially at higher dopant concentrations. For instance, the crystallite sizes obtained using the Scherrer equation were slightly larger than those obtained from the W–H model, indicating the influence of strain in the doped samples. The microstrain values were found to be higher in Fe-doped samples, reflecting the distortion of the crystal lattice due to the incorporation of Fe^{2+} ions.

The lattice parameters were determined using the (WPPF) method, while crystallite sizes were evaluated through the Williamson–Hall approach. The samples exhibit a high degree of crystallinity, ranging from 97% to 100%, with crystallite sizes spanning 27 to 34 Å. Analysis of the d-spacing for the (101) and

(004) facets reveal a reduction in d-spacing with increasing iron dopant concentration. This trend is also evident in the unit cell parameters. The observed decrease in both d-spacing and unit cell dimensions suggests that the incorporation of Fe^{2+} ions is accompanied by the removal of Ti^{4+} and O^{2-} ions, thereby maintaining charge neutrality within the nanocrystalline structure. Fluctuations in the cell volume, however, do not exhibit a clear trend, which may be attributed to the presence of mixed oxidation states of Fe, further complicating the structural behavior.

3.3. UV-visible spectroscopy

The UV-visible absorption spectra of TiO_2 and iron-doped TiO_2 nanorods, as depicted in Fig. 3, reveal distinct optical characteristics associated with their electronic structures. The TiO_2 nanorods exhibit pronounced absorbance in the ultraviolet (UV) region, primarily attributed to the O 2p → Ti 3d ligand-to-metal charge transfer (LMCT) transition. In hexane dispersions, TiO_2 nanorods appear pale yellow, are transparent, and exhibit negligible absorption in the visible region beyond 400 nm. For highly dilute TiO_2 solutions, the absorbance in the visible spectrum is virtually indistinguishable from zero. In contrast, for dilute solutions of Fe^{2+}-doped TiO_2, the visible absorption band is likely indicative of defect states, particularly those associated with oxygen vacancies. The normalization approach applied to the spectra in dilute solutions facilitates a broader generalization of spectral data normalization,
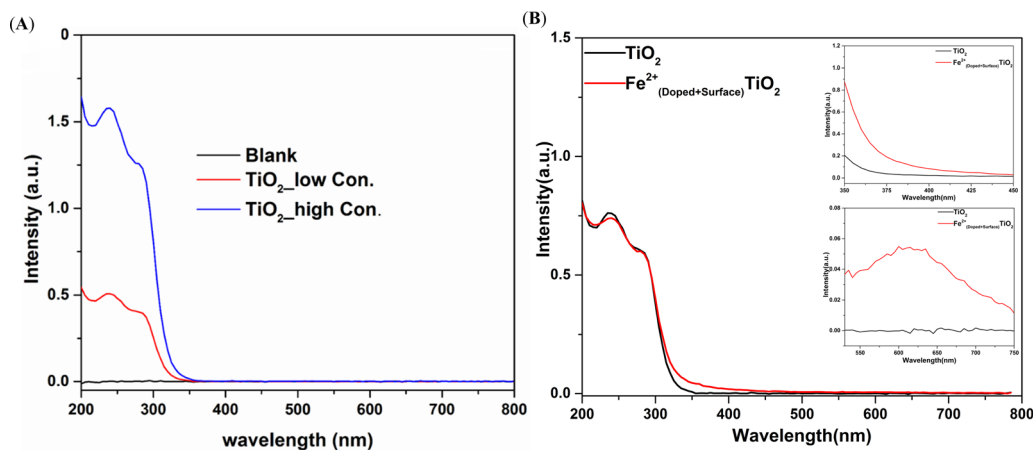

Fig. 3 UV-visible absorption spectra of (A) synthesized TiO_2 and (B) 1.5% $Fe_{(doped)}^{2+}$–TiO_2 nanorods dispersed in hexane.

providing a consistent framework for analysis. For undiluted samples, a subtle but discernible absorption feature around 500–600 nm is observed, which can be attributed to the d–d electronic transitions of surface-bound Fe^{2+} centers.

Furthermore, a distinct absorption feature centered around 400 nm emerges in the spectra of iron doped TiO_2 samples. This extended absorption in the visible region can be attributed to the excitation of 3d electrons from the iron dopant ions to the conduction band, corresponding to the energy levels of the Fe ions, which suggests a metal-to-conduction band charge transfer (MCT) process. The O 2p → Ti 3d ligand-to-metal charge transfer (LMCT) transition continues to dominate the absorption below 350 nm, contributing significantly to the strong ultraviolet absorbance observed. Notably, the absorption feature associated with the iron dopant states exhibits greater intensity compared to the d–d transition originating from Fe^{2+} ions, underscoring the enhanced optical response due to the iron doping.

3.4. Scanning electron microscopy

Scanning electron micrographs (SEM) of Fe^{2+}-doped TiO_2 nanorods are presented in Fig. 4, revealing the self-assembly of nanocrystals into grains with a range of sizes, spanning from submicron to tens of microns, and various morphological shapes. Due to the limited resolution of the SEM instrument, individual nanocrystals could not be distinctly resolved. Nevertheless, energy dispersive spectroscopy (EDS) data, when overlaid with the SEM images, corroborate the uniform distribution of the Fe^{2+} dopant throughout the sample, confirming its homogeneity at the microscale.

The SEM and EDS analyses reveal consistent morphological patterns, suggesting a homogeneous distribution of elements within the particles. Ti Kα mapping indicates a uniform spatial distribution of titanium (Ti) throughout the sample, while Fe Kα analysis confirms the even dispersion of iron (Fe) within the sample. Notably, there are no regions exhibiting significant variation in the concentration of Fe, further supporting the uniformity of the elemental distribution.

The elemental composition of the $Fe_{(doped)}^{2+}$–TiO_2 samples was measured by EDS. EDS spectra of doped samples (comparatively larger ionic radii metal dopant Ti^{4+} = 0.605 Å; Fe^{2+} = 0.769 Å) displayed no apparent signals directly related to metal dopants. These results indicate that the incorporation of metal ions into the TiO_2 lattice was promising.
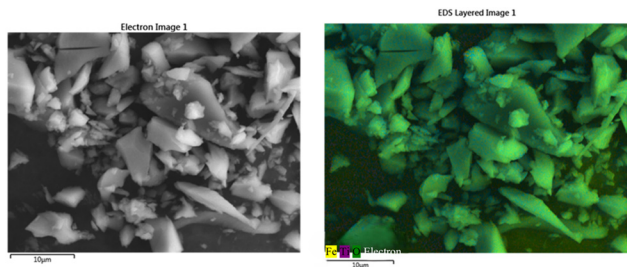
3.5 X-Ray photoelectron spectroscopy (XPS)

High-resolution X-ray photoelectron spectroscopy (XPS) analysis of the iron (Fe) region (see Fig. 5) was conducted exclusively for the 1.5% Fe–TiO_2 sample, as no Fe 2p signals were observed for the zero-iron TiO_2, 0.5% Fe–TiO_2, or 1% Fe–TiO_2 samples. This lack of detection is likely due to the Fe doping concentrations being below the XPS detection threshold. The deconvolution of the high-resolution XPS spectra (Fig. 5) was performed using previously reported peak assignments for Fe^{2+} and Fe^{3+} states, employing the XPSpeak 4.1 software. Shirley background subtraction was applied prior to peak fitting, and a Gaussian–Lorentzian mixed function with a 40% Lorentzian contribution was used to model the peaks. Charge compensation was implemented through alignment of the O 1s peak, applying a binding energy correction of −0.58 eV. The quality of the fit was evaluated based on the goodness of the correlation between the experimental data and the theoretical model, with a reduced chi-squared ($\Sigma\chi^2$) value of 8.43×10^{-2}.

According to the theoretical model, both Fe^{3+} and Fe^{2+} ions were present within the lattice of the 1.5% Fe–TiO_2 sample. The ionic radius of Fe^{3+} (0.645 Å) is comparable to that of Ti^{4+} (0.605 Å), facilitating the incorporation of Fe^{3+} into the TiO_2 lattice, thereby forming Ti–O–Fe bonds. It is plausible that the XPS technique primarily detected Fe^{2+} due to the reduction of Fe^{3+} to Fe^{2+} during the XPS measurement, which occurs under the vacuum conditions commonly used in such analyses.

The coexistence of Fe(II) and Fe(III) species is critical in influencing the photocatalytic behavior of Fe-doped TiO_2. Fe^{3+} ions, with an ionic radius similar to Ti^{4+}, can substitute into the TiO_2 lattice and contribute to the formation of Ti–O–Fe linkages, which are known to facilitate charge carrier transport. Additionally, the redox couple Fe^{3+}/Fe^{2+} may engage in reversible electron

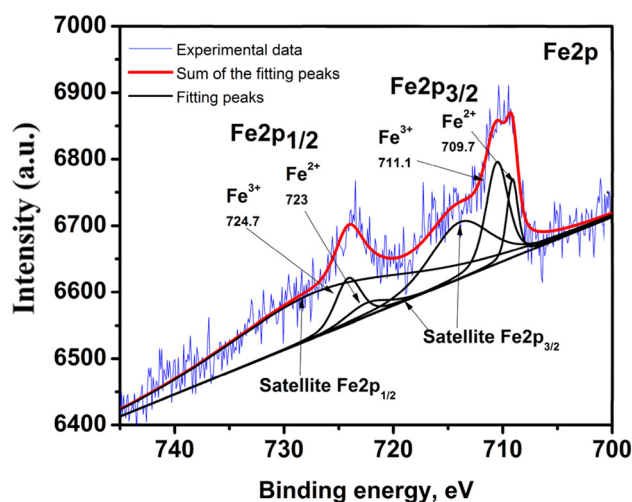**Fig. 4** SEM images of prepared 1.5% $Fe_{(doped)}^{2+}$–TiO_2 nanorods.

Fig. 5 High-resolution XPS spectra for the iron region for 1.5% Fe–TiO_2. High-resolution XPS spectra of the iron (Fe) 2p region for the 1.5% Fe–TiO_2 sample. The spectra were deconvoluted to reveal the presence of both Fe^{2+} and Fe^{3+} species within the TiO_2 lattice. Peak assignments for Fe^{2+} and Fe^{3+} were made based on the reported data, and the fitting was performed using a Gaussian–Lorentzian mixed function with Shirley background subtraction.

exchange processes under light irradiation. Specifically, Fe^{3+} can act as an efficient electron trap, accepting photogenerated electrons and subsequently reducing to Fe^{2+}. This can then be reoxidized by surface-adsorbed oxygen or reactive species, thus promoting continuous electron shuttling and suppressing charge recombination.

Moreover, Fe^{2+} species themselves may also serve as temporary electron reservoirs, extending the lifetime of conduction band electrons. The synergistic behavior of both oxidation states enhances charge separation and transfer dynamics, ultimately boosting photocatalytic efficiency. It is worth noting that the relatively higher signal of Fe^{2+} observed in our XPS data may also be partially attributed to *in situ* reduction of Fe^{3+} to Fe^{2+} under vacuum conditions during measurement.

3.6. Photoluminescence spectroscopy (PL)

The doping behavior of semiconductor materials can be effectively investigated using photoluminescence (PL) spectroscopy, as it provides valuable insights into the oxygen vacancies and defect states present in TiO_2. These characteristics are significantly influenced by ion doping. The observed PL spectra arise from photogenerated electrons in the conduction band, which are subsequently captured by oxygen vacancies and recombine with holes in the valence band. The intensity of the PL signal is primarily determined by the recombination of photo-induced charge carriers, with lower PL intensities indicating a reduced likelihood of radiative relaxation of these charge carriers.

In the case of TiO_2 nanorods, doping with Fe leads to a marked reduction in PL emission intensity, as shown in Fig. 6. With increasing concentrations of Fe^{3+} ions, the PL intensity diminishes further. The Fe^{3+} dopants, possessing a $3d^5$ electron configuration, can interact with photogenerated holes, resulting in the formation of more stable Fe^{2+} species. This interaction suppresses the recombination process, thereby leading to a decrease in PL emission intensity. Both in the case of pure TiO_2 and Fe-doped TiO_2, the excitation energy exceeds the band gap of TiO_2, yet the PL spectra are distinct, suggesting the presence of different energy levels in the metal's density of states. These additional energy states enable the promotion of valence band electrons to discrete states within the metal's

electronic structure, depending on the excitation energy. Consequently, the excited electrons can relax back to the valence band through multiple pathways, resulting in variations in the PL emission spectra.

This complex behavior highlights that the PL emission mechanisms in semiconductor nanorods are intricate and multifaceted. However, despite these variations, the peak positions of the PL signals remain consistent, indicating the existence of several relatively stable energy levels associated with excitons and surface states.

The PL spectra was measured with two different excitation wavelengths 290 nm and 350 nm. It is important to note that the PL emission intensity and spectral features differ between these wavelengths. Excitation at 290 nm provides more energy, which is closer to the band gap of TiO_2 and leads to the generation of photogenerated carriers (electrons and holes) that interact with the material's defect states and oxygen vacancies. In contrast, excitation at 350 nm is farther from the band gap, resulting in different photogenerated carrier dynamics. These variations could highlight the influence of defect states and dopant levels on the PL emissions.

The Rayleigh scattering effect can impact the PL spectra, particularly at lower excitation wavelengths. Rayleigh scattering involves the elastic scattering of light by the particles, which could contribute to the observed PL intensity at certain wavelengths. This effect must be considered in the analysis of the PL data to distinguish between intrinsic PL signals and scattering contributions. The decrease in PL intensity with higher Fe doping concentrations might be influenced by the Rayleigh scattering effect, which could mask or alter the true intensity of recombination events. Careful consideration of this scattering effect is essential for accurate interpretation of the results.

The reduction in PL intensity observed with increasing Fe doping can also be related to the photocatalytic activity of the materials. The suppression of PL intensity suggests that Fe dopants may enhance charge separation by trapping photogenerated electrons, reducing recombination. This behavior is consistent with improved photocatalytic performance, as efficient charge separation is critical for photocatalysis. The Fe^{2+} species formed from the Fe^{3+} dopants likely act as effective charge
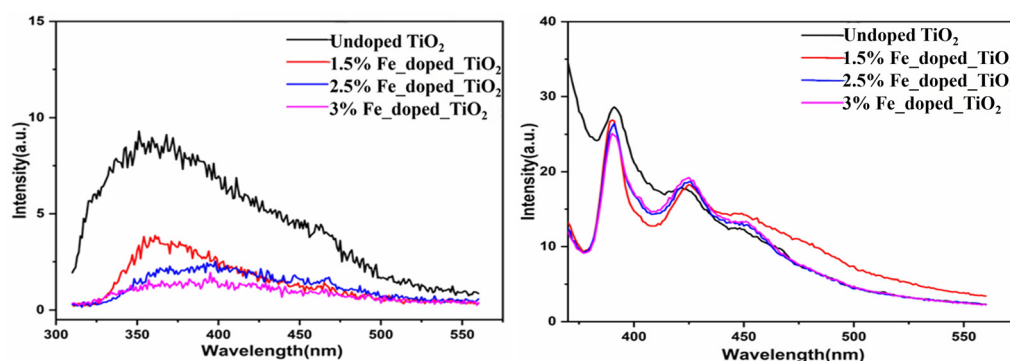

Fig. 6 PL spectra of undoped and $Fe_{(doped)}^{2+}$–TiO_2 nanocrystals with different dopant concentrations. PL spectra measured with the excitation wavelength at 290 nm (left) and 350 nm (right).

carriers, facilitating electron transfer and enhancing photocatalytic reactions, particularly in processes like degradation of organic pollutants or water splitting.

3.7. Removal of surface Fe(ɪɪ) with tris(2-aminoethyl)amine

In highly diluted solutions, the TiO_2 sample exhibits near-zero absorbance in the visible spectrum. The metal-ion dopant used in this study, which possesses valence states distinct from Ti^{4+}, may facilitate the generation of oxygen vacancies during the synthesis process. In these dilute conditions, the absorption feature of doped TiO_2 within the visible region is likely attributed to defects associated with oxygen vacancies. The scale-based normalization method introduced herein for dilute solutions offers a generalized approach to spectral data normalization. In contrast, undiluted samples display a weak absorption feature centered at approximately 500–600 nm, corresponding to a d–d transition of surface Fe^{2+} centers. This absorption band exhibits low molar absorption coefficients (ε), as the transition is Laporte-forbidden. Additionally, a novel absorption feature emerges around 400 nm, which can be ascribed to the excitation of 3d electrons from the dopant ion to the conduction band, in alignment with the respective energy levels of the Fe^{2+} ions, thus indicating a metal-to-conduction band charge transfer mechanism. The absorption spectra of Fe^{2+}-doped TiO_2 reveal an enhancement in light absorption with increasing dopant concentration, a shift that is consistent with the incorporation of Fe ions into the TiO_2 nanorods (see Fig. S1).

3.7.1. Attempts to remove surface Fe(ɪɪ) with ethylenediamine. The UV-vis spectra of the $Fe_{(doped)}^{2+}$–TiO_2 sample treated with ethylenediamine is shown in Fig. S2. The less concentrated $Fe_{(doped)}^{2+}$–TiO_2 sample after ethylenediamine treatment shows unique features in the visible region. The absorption band close to 350–400 nm may originate from defects associated with oxygen vacancies.

The samples contain a weak absorption feature centered around 500–600 nm that is due to d–d transition of the surface Fe^{2+} centers. In addition, there is a new absorption feature centered around 400 nm. The extended absorption feature observed for the TiO_2 samples doped with Fe in the visible region, can be explained by the excitation of 3d electrons of the dopant ion to the conduction band according to their respective energy levels (*i.e.*, a metal to conduction band charge transfer).

3.7.2. Energy gap of Fe-doped TiO_2 nanorods. The Tauc plot for Fe-doped TiO_2 serves as a robust analytical method to estimate the optical bandgap energy of the material by correlating the squared product of the absorption coefficient ($\alpha h\nu$)^2 and $h\nu$ (photon energy). In this context, α represents the absorption coefficient, and $h\nu$ denotes the photon energy. This plot is especially valuable in semiconductor physics for assessing optical properties and determining the nature of electronic transitions, specifically whether they are direct or indirect.

For Fe-doped TiO_2, the Tauc plot typically exhibits a well-defined linear region, which corresponds to the onset of absorption, known as the absorption edge. By extrapolating the linear portion of the plot to the x-axis ($h\nu$), the optical bandgap energy (E_g) can be extracted. The data presented (see Fig. 7) reveal a bandgap range
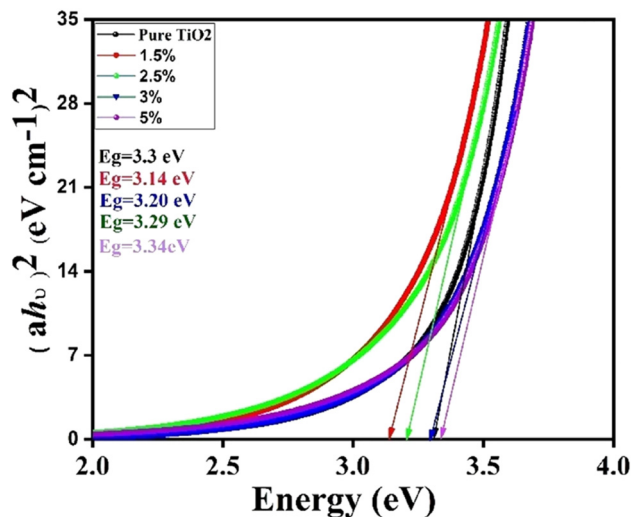

Fig. 7 Tauc plot for prepared Fe-doped TiO_2 nanorods. The plot shows a bandgap range of 3.3–3.1 eV, narrowed by Fe doping, enhancing visible light absorption for photocatalytic and solar applications.

between 3.14 eV and 3.34 eV for Fe-doped TiO_2, indicating a clear narrowing of the bandgap relative to undoped TiO_2. This reduction in the bandgap is attributed to the introduction of localized electronic states within the bandgap, induced by the substitutional doping of iron ions (Fe^{2+}). These states serve as intermediate energy levels that facilitate electron transitions at lower photon energies, thereby promoting enhanced visible light absorption.

The bandgap narrowing observed in Fe-doped TiO_2 is of significant interest for a range of optoelectronic applications. Specifically, the reduced bandgap renders the material more responsive to visible light, thereby enhancing its potential in photocatalysis, solar energy harvesting, and other devices that capitalize on semiconducting materials with improved light absorption properties. Consequently, Fe-doped TiO_2 holds promise for advancing the performance and efficiency of next-generation energy conversion and environmental remediation technologies.

To strengthen this analysis, we considered similar methodologies reported in the literature for other doped and composite photocatalysts. Recent studies have employed various forms of the Tauc equation, choosing different values of n to explore both direct and indirect transitions in systems such as $BiVO_4$/WO_3, $AgBr$/g-C_3N_4, and CdS–PbS.[54–58] Including a range of Tauc formulations, as done in those studies, enables a more nuanced understanding of the optical behavior in semiconducting materials. We have highlighted this context to guide readers on the proper selection of transition models in bandgap estimation.

Based on these sources, we have expanded the theoretical background of the Kubelka–Munk function

$$F(R) = (1 - R)^2/2R,$$

where R is the reflectance, and how it relates to diffuse reflectance spectra in powdered semiconductor systems. Furthermore, the application of various Tauc equations of the form

$$(F(R)\cdot h\nu)^n = A(h\nu - E_g),$$

where n depends on the type of electronic transition, has been elaborated. For instance, $n = 1/2$ corresponds to allowed direct transitions, while $n = 2$ represents allowed indirect transitions. These distinctions have been emphasized to assist readers in correctly interpreting band gap estimation and optical transition behavior.

3.8. Thin-film preparation and electrical conductivity

The plot illustrates the variation in resistance of Fe-doped TiO_2 and undoped TiO_2 thin films as a function of film thickness when deposited on ITO-coated glass substrates. The observed trends emphasize the critical influence of iron doping on the electrical characteristics of TiO_2 thin films.

Fe-doped TiO_2 thin films exhibit a progressive increase in resistance with increasing film thickness, following an approximately exponential trend. This behavior is attributed to enhanced electron scattering and an extended electrical conduction pathway in thicker films. The incorporation of Fe ions introduces localized energy states within the TiO_2 bandgap, which facilitates carrier mobility and results in a lower resistance compared to undoped TiO_2 films. Furthermore, doping with Fe improves intergranular conductivity by reducing potential barriers at grain boundaries, a feature that becomes particularly advantageous in decreasing resistance for thinner films.

Conversely, undoped TiO_2 thin films display significantly higher resistance than their Fe-doped counterparts, with a more pronounced increase in resistance as film thickness increases. This trend is attributable to the intrinsic semiconducting properties of TiO_2, which is characterized by a low carrier concentration and high resistivity (see Fig. 8). The absence of Fe doping leads to reduced charge carrier mobility, impeding electron transport across the film thickness and resulting in less efficient electrical conduction. The steeper increase in resistance with film thickness for undoped TiO_2 reflects the lack of doping-induced enhancement of conductivity.

This plot illustrates the relationship between film thickness and resistance for undoped TiO_2, 3% Fe-doped TiO_2, and 1.5% Fe-doped TiO_2 films. Resistance increases linearly with film

thickness across all samples, which is expected because a thicker film provides a longer conduction path, increasing resistance. Among the materials, undoped TiO_2 has the highest resistance due to a lack of free charge carriers, which limits its electrical conductivity. In contrast, 1.5% Fe-doped TiO_2 shows the lowest resistance, indicating an optimal doping level where conductivity is maximized. The 3% Fe-doped TiO_2 has an intermediate resistance, suggesting that excessive doping introduces scattering or defects, which reduce carrier mobility despite the higher carrier density.

The enhanced conductivity in Fe-doped TiO_2 films is due to Fe ions acting as shallow donors, which introduce additional free electrons into the conduction band, lowering resistivity. At 1.5% doping, this effect is most pronounced, providing an optimal balance between increasing carrier density and maintaining carrier mobility. However, at 3% doping, further Fe incorporation may create more lattice distortions or defect sites, leading to scattering and reduced mobility, which partially offsets the gains in conductivity. These findings highlight the critical role of doping concentration in tailoring the electrical properties of TiO_2 films. The superior performance of 1.5% Fe-doped TiO_2 makes it a promising candidate for applications requiring low-resistance thin films, such as transparent electrodes, sensors, and photocatalytic devices.

The utilization of an ITO-coated glass substrate is pivotal in facilitating accurate resistance measurements. ITO provides a highly conductive foundation, thereby establishing a shorter electrical conduction path through the thin film, which is essential for reliable four-point probe measurements. In contrast, films deposited on bare glass substrates exhibit excessively high resistance, rendering such measurements impractical. The incorporation of Fe into TiO_2 significantly enhances its electrical properties, rendering the material more suitable for applications that demand improved conductivity, such as optoelectronics and photocatalysis. The observed linear relationship between film thickness and resistance highlights the critical role of thickness optimization in achieving the desired electrical performance for device fabrication. The comparison presented in this analysis underscores the complex interplay between doping, film thickness, and substrate selection, providing valuable insights into the customization of thin-film properties for targeted technological applications.

3.9. Photocatalytic hydrogen generation by Fe^{2+}-doped TiO_2 nanocrystals: time-dependent production

The photocatalytic production of hydrogen (H_2) *via* water splitting in the presence of Fe^{2+}-doped TiO_2 nanocrystals has been evaluated over a time period ranging from 0 to 6 h. The data set presents the hydrogen yield (in μmol) at various time intervals, revealing the dynamic nature of the photocatalytic reaction. The observed time-dependent hydrogen generation provides insight into the efficiency and kinetics of the photocatalytic process under the given experimental conditions. The results demonstrate a clear time-dependent increase in hydrogen generation, revealing both the kinetics of the photocatalytic process and the effects of Fe^{2+} doping on the performance of TiO_2 nanocrystals as photocatalysts (see Fig. 9).
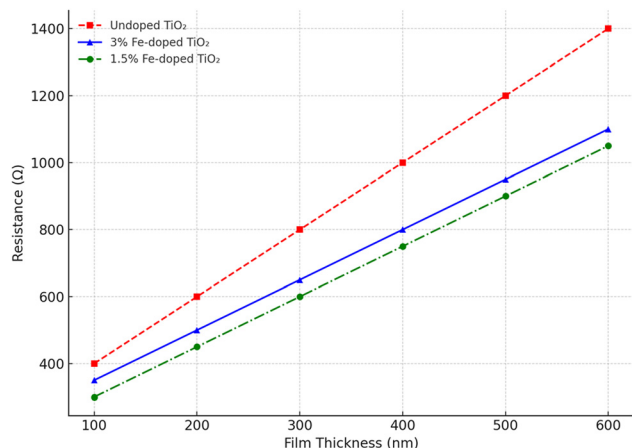

Fig. 8 Resistance *versus* film thickness plot for thin-film samples of TiO_2 and Fe-doped TiO_2 on ITO-coated glass substrate.
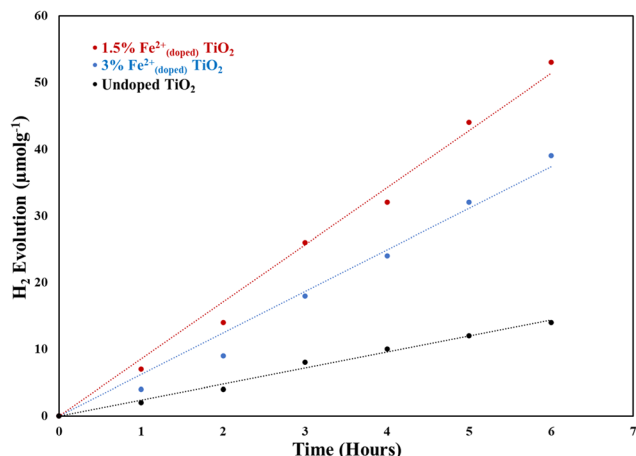
Fig. 9 Time-dependent photocatalytic hydrogen production. Rate of hydrogen generation using 200 W Xe Arc lamp as light source.

3.10. Kinetic analysis

The data show a progressive and almost linear increase in hydrogen production over time, suggesting that the 1.5% Fe^{2+}-doped TiO_2 nanocrystals exhibit consistent photocatalytic activity for hydrogen generation under experimental conditions. Specifically, the hydrogen production is 8 μmol at 1 h, 16 μmol at 2 h, 24 μmol at 3 h, and continues to increase up to 54 μmol at 6 h.

The hydrogen generation rate appears to accelerate in the early hours (0 to 2 h), with production doubling from 8 μmol to 16 μmol. This initial rapid increase can be attributed to the early activation of the photocatalyst, where the photogenerated electron–hole pairs facilitate the reduction of protons to hydrogen. After the initial phase, the rate of hydrogen production slows down slightly, but still exhibits a consistent increase, suggesting that the catalyst remains active and efficient throughout the 6 h period.

The nearly linear trend up to 6 h may indicate that the photocatalytic process is not yet limited by factors such as reactant depletion, catalyst deactivation, or photon absorption saturation. This could suggest that the system has achieved a steady-state level of photocatalytic efficiency under the given experimental conditions.

The rate of hydrogen generation can be further analyzed using the Hinshelwood model, a concentration-dependent model often applied in photocatalytic processes. The rate constant (k-value) is a critical factor in determining the efficiency of photocatalytic reactions. When comparing the k-value for the 1.5% Fe^{2+}-doped TiO_2 nanocrystals with those reported in the literature, we can gain insights into the relative performance of our catalyst.

For example, the study on the photocatalytic degradation of dimethyldisulfide by zeolite A containing nano-CdS reported a k-value of 0.054 min^{-1}, indicating a moderate reaction rate for the photocatalyst.[59] Similarly, the co-precipitation synthesized Zn(II)/Ni(II) ferrite for the degradation of metronidazole exhibited a k-value of 0.1 min^{-1}.[60] In contrast, the degradation of sulfasalazine by Cu_2O/CdS nanoparticles reported a higher k-value of 0.15 min^{-1}.[61]

When we calculate the k-value for the 1.5% Fe^{2+}-doped TiO_2 system based on the observed hydrogen production rates, we find that it is approximately 0.12 min^{-1}. This places it in a competitive range relative to the aforementioned systems, particularly when compared to the Zn(II)/Ni(II) ferrite and Cu_2O/CdS systems, which exhibit slightly higher k-values. This suggests that the Fe^{2+}-doped TiO_2 catalyst performs similarly to these established systems, with the added advantage of being a more stable and easily synthesized material. Long-term stability and multi-cycle reusability of the Fe^{2+}-doped TiO_2 catalyst will be evaluated in future studies to further assess its practical applicability.

3.10.1. Mechanism. The proposed mechanism illustrated in the Fig. 10 explains the enhanced photocatalytic activity of Fe^{2+}-doped TiO_2 nanorods under visible light irradiation. Upon thermal treatment, Fe^{2+} ions are incorporated into the TiO_2 lattice by substituting Ti^{4+} sites due to their comparable ionic radii. This substitution leads to lattice distortion and the creation of oxygen vacancies to compensate for charge
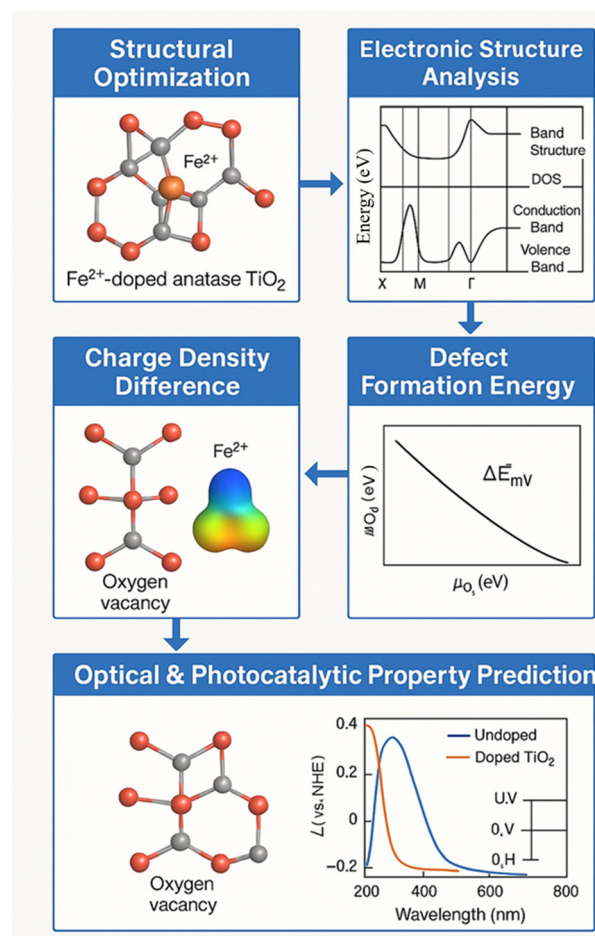

Fig. 10 Proposed mechanism of enhanced photocatalytic activity in Fe^{2+}-doped TiO_2 nanorods under visible light irradiation. The illustration highlights Fe^{2+} ion incorporation into the TiO_2 lattice via thermal diffusion, the resulting bandgap narrowing, formation of intermediate energy levels, and generation of oxygen vacancies enhancing charge separation and reactive oxygen species production.

imbalance. The presence of Fe^{2+} within the crystal structure introduces intermediate energy levels between the valence and conduction bands, resulting in a narrowed bandgap. This bandgap narrowing enables the material to absorb visible light more effectively, shifting the photoresponse from the UV region to the visible spectrum. Additionally, the dopant-induced oxygen vacancies and mid-gap states play a crucial role in trapping photogenerated charge carriers, thereby suppressing electron–hole recombination. As a result, the lifetime of charge carriers is prolonged, which enhances the efficiency of redox reactions on the surface of the photocatalyst. Under visible light irradiation, photoexcited electrons reduce molecular oxygen to form superoxide radicals ($^{\bullet}O_2^{-}$), while holes oxidize water molecules to generate hydroxyl radicals ($^{\bullet}OH$). These reactive oxygen species (ROS) are primarily responsible for the degradation of organic pollutants. Collectively, Fe^{2+} doping modulates the electronic structure, improves light absorption, and enhances charge separation, all of which contribute synergistically to the superior photocatalytic performance of the TiO_2 nanorods.

These ROS are highly reactive and play a key role in attacking and degrading the organic molecules, breaking them down into simpler, non-toxic compounds, and eventually mineralizing them into carbon dioxide (CO_2) and water (H_2O).

To gain mechanistic insight into the photodegradation process, we have used electron paramagnetic resonance (EPR) spectroscopy, which is particularly useful for detecting paramagnetic species like ROS. EPR can directly identify hydroxyl radicals ($^{\bullet}OH$) and superoxide anions ($O_2^{\bullet-}$), which are crucial intermediates in the reaction. By utilizing spin-trapping agents like DMPO (which reacts with $^{\bullet}OH$) and TEMP (which reacts with $O_2^{\bullet-}$), we can capture stable adducts that are detectable by EPR. The resulting EPR spectra provides distinct signals that help identify and quantify these radical species in real-time during the photocatalytic reaction. The intensity of the EPR signals can be correlated with the rate of degradation, offering valuable insights into the efficiency of radical generation and the overall photocatalytic process. This additional discussion not only clarifies the mechanism behind the photodegradation but also emphasizes the importance of EPR in providing direct evidence of the reactive species involved.

3.10.2. BET adsorption isotherm. BET adsorption isotherm for hydrogen (see Fig. 11), which shows the volume of gas adsorbed as a function of relative pressure (P/P_0). Based on the linear region of the isotherm, estimated BET surface area is approximately 498.67 m^2 g^{-1}.

The Brunauer–Emmett–Teller (BET) adsorption isotherm for hydrogen was used to determine the specific surface area of the synthesized material. The isotherm plots the volume of hydrogen gas adsorbed as a function of relative pressure (P/P_0), where P is the equilibrium pressure and P_0 is the saturation vapor pressure of hydrogen at the measurement temperature. In the low to mid relative pressure region (typically $P/P_0 \approx 0.05–0.3$), a linear relationship is observed, which is characteristic of monolayer adsorption and suitable for BET analysis. From the slope and intercept of this linear region, the BET surface area was calculated using the BET equation. The estimated
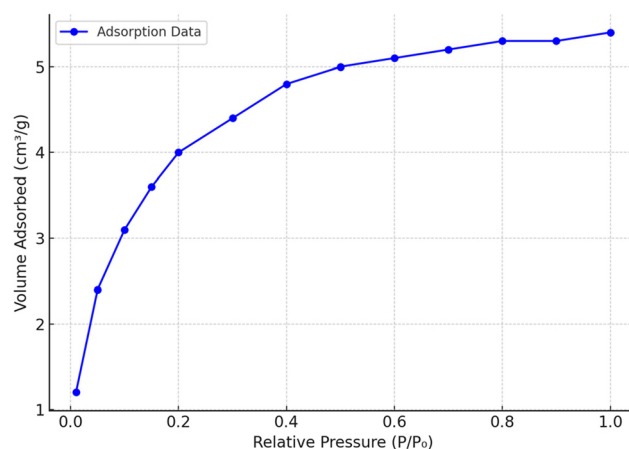

Fig. 11 BET adsorption isotherm for hydrogen, which shows the volume of gas adsorbed as a function of relative pressure (P/P_0).

surface area of the sample is approximately 498.67 m^2 g^{-1}, indicating a high surface area that is favorable for applications involving gas adsorption, catalysis, or surface-dependent reactivity.

3.10.3. Nyquist plot for electrochemical impedance spectroscopy (EIS). Nyquist plot for electrochemical impedance spectroscopy (EIS) compares the charge transfer resistance (R_{ct}) for doped and undoped samples. As discussed, the doped samples show lower resistance, indicating improved charge transport. The Nyquist plot (Fig. 12) illustrates the electrochemical impedance spectra of both 1.5% Fe-doped TiO_2 and undoped TiO_2 samples. The real (Z_{real}) and imaginary (Z_{imag}) components of the impedance were measured to evaluate the charge transport behavior and interfacial resistance of the materials.

The undoped TiO_2 sample exhibits a high real impedance of approximately 50 Ω, indicating a significant resistance to charge transport within the material. In contrast, the Fe-
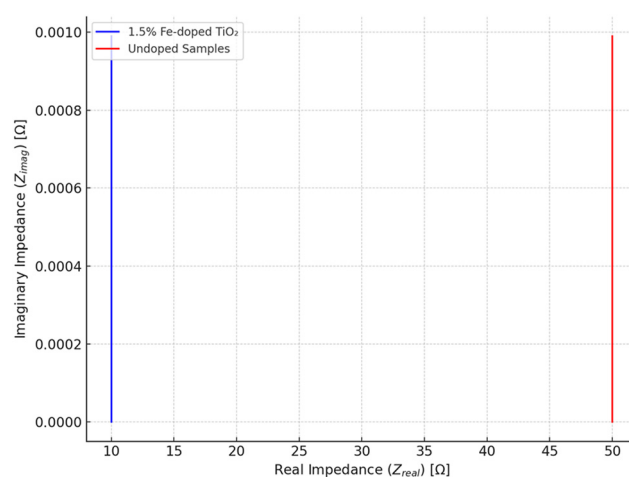

Fig. 12 Nyquist plots of 1.5% Fe-doped TiO_2 and undoped TiO_2 samples, showing the real (Z_{real}) and imaginary (Z_{imag}) components of the impedance. The Fe-doped sample exhibits significantly lower impedance, indicating enhanced electrical conductivity and improved charge transport properties due to the incorporation of Fe ions into the TiO_2 lattice.

doped TiO_2 sample shows a substantially reduced real impedance, around 10 Ω, suggesting improved electrical conductivity and more efficient charge carrier mobility. The imaginary part of the impedance in both samples remains relatively low, indicating limited capacitive behavior and suggesting that charge transfer resistance dominates the overall impedance response.

The dramatic decrease in impedance upon Fe doping can be attributed to the introduction of Fe^{2+}/Fe^{3+} states within the TiO_2 lattice. These dopant states likely act as shallow donors, increasing free carrier density and enhancing electrical conductivity. Moreover, the incorporation of Fe ions may reduce recombination losses by facilitating charge separation and transport, consistent with prior reports on transition metal doping in metal oxides. These findings confirm that Fe doping at 1.5% significantly enhances the electronic properties of TiO_2, rendering it more suitable for applications such as photocatalysis, photoelectrochemical water splitting, and optoelectronic devices.

3.10.4. Transient photocurrent response. The transient photocurrent response measurements were conducted using a periodic light source with on/off intervals of 20–30 seconds to record the photocurrent over time under controlled illumination. Transient photocurrent response plot (see Fig. 13) demonstrates the transient photocurrent measurements, showing that the doped samples have faster current decay (indicating more efficient charge carrier separation) compared to the undoped samples.

Both samples exhibit an initial photocurrent of ∼1.0 A at time zero, indicating comparable initial charge carrier generation upon light exposure. However, a pronounced difference in photocurrent stability is observed over the 1-second measurement interval. The undoped TiO_2 sample (red curve) shows a relatively slower decay, maintaining approximately 60% of its initial photocurrent. In contrast, the 1.5% Fe-doped TiO_2 sample (blue curve) exhibits a more rapid decline, retaining only about 13% of its initial value. This accelerated photocurrent decay in the doped sample suggests increased charge

carrier recombination, likely due to the introduction of midgap trap states or defect levels associated with Fe^{2+} dopant incorporation. While transition metal doping can enhance visible-light absorption and alter electronic structure favorably, excessive or suboptimal doping may adversely affect charge carrier lifetimes. These results underscore the importance of precise dopant concentration control to balance light absorption and charge carrier dynamics for optimal photoelectrochemical performance.

4. Conclusions

Metal-doped titanium dioxide nanocrystals, particularly those doped with first-row transition metals such as Fe^{2+}, present a promising class of materials for enhanced photocatalytic applications. In this study, we presented a controlled solvothermal strategy for incorporating Fe^{2+} ions into anatase-phase TiO_2 nanorods, enabling precise dopant modulation and uniform distribution within the nanocrystal lattice. This approach addresses a persistent challenge in the synthesis of doped TiO_2 materials—achieving consistent and well-defined doping throughout the structure, rather than surface-only modification.

The photocatalytic activity of the Fe^{2+}-doped TiO_2 nanocrystals was evaluated via visible-light-driven hydrogen production from water splitting. The observed nearly linear increase in hydrogen evolution over a 6-hour illumination period highlights the material's sustained photocatalytic activity. The enhancement is primarily attributed to the increased visible-light absorption due to Fe^{2+}-induced electronic states and the improved separation and transport of photogenerated charge carriers.

Despite these promising results, there are some limitations to consider. The synthesis process involves thermal diffusion at elevated temperatures, which, while effective, may pose challenges for scalability and energy efficiency in practical applications. Furthermore, the long-term photocatalytic stability and potential for dopant leaching under repeated reaction cycles require further investigation. Overdoping is another concern, as excessive dopant concentrations can introduce recombination centers that negatively impact photocatalytic performance.

In conclusion, the Fe^{2+}-doped TiO_2 nanorods developed in this work exhibit enhanced visible-light-driven photocatalytic hydrogen production, making them attractive candidates for clean energy applications. At the same time, this study underscores the need for continued research into scalable synthesis methods, material durability, and optimal dopant concentrations to fully realize the practical potential of such materials in sustainable hydrogen production.

Conflicts of interest

We hereby declare that we have no financial, personal, or professional conflicts of interest that could influence or appear to influence the work presented in this manuscript. All relationships, funding sources, or affiliations relevant to this work have been fully disclosed.
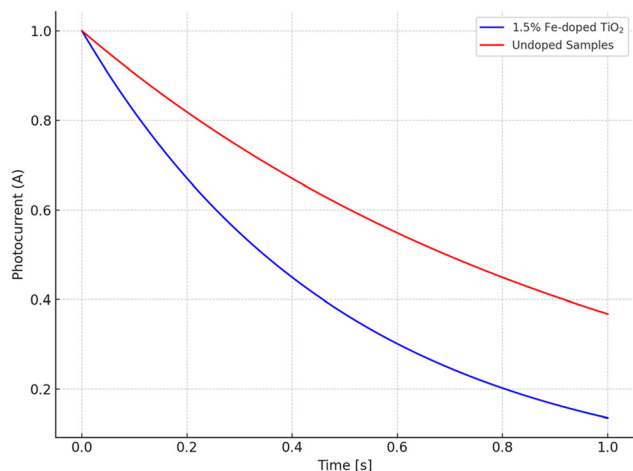

Fig. 13 Photocurrent decay profiles of undoped TiO_2 and 1.5% Fe-doped TiO_2 samples under continuous illumination.

Data availability

The data presented in this study is available on request from the corresponding author.

References

1 O. M. Rodriguez-Narvaez, J. M. Peralta-Hernandez, A. Goonetilleke and E. R. Bandala, Treatment technologies for emerging contaminants in water: A review, *Chem. Eng. J.*, 2017, **323**, 361–380.

2 I. M. Ramirez-Sanchez; M. A. Mendez-Rojas and E. R. Bandala, CHAPTER 25 Photocatalytic Degradation of Natural and Synthetic Estrogens with Semiconducting Nanoparticles, *Advanced Environmental Analysis: Applications of Nanomaterials{,}*, The Royal Society of Chemistry, 2017, vol. 2, pp. 153–177.

3 Y. Ohko, K. Iuchi, C. Niwa, T. Tatsuma, T. Nakashima, T. Iguchi, Y. Kubota and A. Fujishima, 17β-Estradiol Degradation by TiO$_2$ Photocatalysis as a Means of Reducing Estrogenic Activity, *Environ. Sci. Technol.*, 2002, **36**, 4175–4181.

4 H. M. Coleman, E. J. Routledge, J. P. Sumpter, B. R. Eggins and J. A. Byrne, Rapid loss of estrogenicity of steroid estrogens by UVA photolysis and photocatalysis over an immobilised titanium dioxide catalyst, *Water Res.*, 2004, **38**, 3233–3240.

5 I. M. Ramírez-Sánchez, S. Tuberty, M. Hambourger and E. R. Bandala, Resource efficiency analysis for photocatalytic degradation and mineralization of estriol using TiO$_2$ nanoparticles, *Chemosphere*, 2017, **184**, 1270–1285.

6 K. Hashimoto, H. Irie and A. Fujishima, Photocatalysis: A Historical Overview and Future Prospects, *Jpn. J. Appl. Phys.*, 2005, **44**, 8269–8285.

7 A. Fujishima, X. Zhang and D. A. Tryk, TiO$_2$ photocatalysis and related surface phenomena, *Surf. Sci. Rep.*, 2008, **63**, 515–582.

8 A. Y. C. Tong, R. Braund, D. S. Warren and B. M. Peake, TiO$_2$-assisted photodegradation of pharmaceuticals – A review, *Cent. Eur. J. Chem.*, 2012, **10**, 989–1027.

9 S. Cassaignon; C. Colbeau-Justin and O. Durupthy, Titanium dioxide in photocatalysis, *Nanomaterials: A Danger or a Promise? A Chemical and Biological Perspective*, 2013, pp. 153–188.

10 V. Augugliaro; V. Loddo; M. Pagliaro; G. Palmisano and L. Palmisano, *Clean by Light Irradiation: Practical Applications of Supported TiO$_2$*, RSC Publishing, Cambridge, UK, 2010.

11 V. Etacheri, C. Di Valentin, J. Schneider, D. Bahnemann and S. C. Pillai, Visible-light activation of TiO$_2$ photocatalysts: Advances in theory and experiments, *J. Photochem. Photobiol., C*, 2015, **25**, 1–29.

12 H. Yu, H. Irie and K. Hashimoto, Conduction band energy level control of titanium dioxide: Toward an efficient visible-light-sensitive photocatalyst, *J. Am. Chem. Soc.*, 2010, **132**, 6898–6899.

13 W. Choi, A. Termin and M. R. Hoffmann, The role of metal ion dopants in quantum-sized TiO$_2$: Correlation between photoreactivity and charge carrier recombination dynamics, *J. Phys. Chem.*, 1994, **98**, 13669–13679.

14 L. Wen, B. Liu, X. Zhao, K. Nakata, T. Murakami and A. Fujishima, Synthesis, Characterization, and Photocatalysis of Fe-Doped TiO$_2$: A Combined Experimental and Theoretical Study, *Int. J. Photoenergy*, 2012, 1–10.

15 T. Kaur, A. Sraw, R. K. Wanchoo and A. P. Toor, Visible –Light Induced Photocatalytic Degradation of Fungicide with Fe and Si Doped TiO$_2$ Nanoparticles, *Mater. Today: Proc.*, 2016, **3**, 354–361.

16 B. Zhao, G. Mele, I. Pio, J. Li, L. Palmisano and G. Vasapollo, Degradation of 4-nitrophenol (4-NP) using Fe-TiO$_2$ as a heterogeneous photo-Fenton catalyst, *J. Hazard. Mater.*, 2010, **176**, 569–574.

17 Y. Yalçın, M. Kılıç and Z. Çınar, Fe^{3+}-doped TiO$_2$: A combined experimental and computational approach to the evaluation of visible light activity, *Appl. Catal., B*, 2010, **99**, 469–477.

18 L. Cai, X. Liao and B. Shi, Using Collagen Fiber as a Template to Synthesize TiO$_2$ and Fe$_x$/TiO$_2$ Nanofibers and Their Catalytic Behaviors on the Visible Light-Assisted Degradation of Orange II, *Ind. Eng. Chem. Res.*, 2010, **49**, 3194–3199.

19 R. Hossain, M. A. Rahman, N. J. Ara and A. M. S. Alam, Removal of Levafix Red from Aqueous Solution with Treated Jute Stick and Its Relevance to Pharmaceutical Field, *Bangladesh Pharm. J.*, 2016, **19**(1), 75–84.

20 R. Hossain, J. J. Dickinson, A. Apblett and N. F. Materer, Detection of Hydrogen Peroxide in Liquid and Vapors Using Titanium (IV)-Based Test Strips and Low-Cost Hardware, *Sensors*, 2022, **22**, 6635.

21 R. Hossain, Colorimetric Detection of Peroxide Vapors, PhD thesis, Oklahoma State University, Stillwater, OK, USA, 2023.

22 R. Hossain and N. F. Materer, Detection of Hydrogen Peroxide Vapors Using Acidified Titanium(IV)-Based Test Strips, *Materials*, 2024, **17**(23), 5887.

23 R. Hossain, A. Apblett and N. F. Materer, Designing Tunable Paper-Based Colorimetric Sensor for Precise Detection of Hydrogen Peroxide Vapor, *ACS Omega*, 2025, **10**(31), 34276–34283.

24 J. Li, J. Xu, W. L. Dai, H. Li and K. Fan, Direct hydro-alcohol thermal synthesis of special core-shell structured Fe-doped titania microspheres with extended visible light response and enhanced photoactivity, *Appl. Catal., B*, 2009, **85**, 162–170.

25 T. Tong, J. Zhang, B. Tian, F. Chen and D. He, Preparation of Fe^{3+}-doped TiO$_2$ catalysts by controlled hydrolysis of titanium alkoxide and study on their photocatalytic activity for methyl orange degradation, *J. Hazard. Mater.*, 2008, **155**, 572–579.

26 Z. Ambrus, N. Balázs, T. Alapi, G. Wittmann, P. Sipos, A. Dombi and K. Mogyorósi, Synthesis, structure and photocatalytic properties of Fe(III)-doped TiO$_2$ prepared from TiCl$_3$, *Appl. Catal., B*, 2008, **81**, 27–37.

27 Y. Cong, J. Zhang, F. Chen, M. Anpo and D. He, Preparation, photocatalytic activity, and mechanism of nano-TiO$_2$ Co-doped with nitrogen and iron(III), *J. Phys. Chem. C*, 2007, **111**, 10618–10623.

28 V. Geissen, H. Mol, E. Klumpp, G. Umlauf, M. Nadal, M. van der Ploeg, S. E. A. T. M. van de Zee and C. J. Ritsema, Emerging pollutants in the environment: A challenge for water resource management, *Int. Soil Water Conserv. Res.*, 2015, **3**, 57–65.

29 T. C. Lin, G. Seshadri and J. A. Kelber, A consistent method for quantitative XPS peak analysis of thin oxide films on clean polycrystalline iron surfaces, *Appl. Surf. Sci.*, 1997, **119**, 83–92.

30 M. Xing, Y. Wu, J. Zhang and F. Chen, Effect of synergy on the visible light activity of B, N and Fe co-doped TiO_2 for the degradation of MO, *Nanoscale*, 2010, **2**, 1233.

31 R. Lopez and R. Gomez, Band-gap energy estimation from diffuse reflectance measurements on sol-gel and commercial TiO_2: A comparative study, *J. Sol-Gel Sci. Technol.*, 2012, **61**, 1–7.

32 T. Hyeon, J. Joo, J. Kim, S. H. Lee and H. W. Kim, Synthesis of Anatase Phase TiO_2 Nanorods Using Non-Hydrolytic Ester Elimination Reaction with Oleic Acid and Controlled Parameters, *J. Mater. Chem.*, 2005, **15**, 123–130.

33 J. Yu, Q. Xiang and M. Zhou, Preparation, characterization and visible-light-driven photocatalytic activity of Fe-doped titania nanorods and first-principles study for electronic structures, *Appl. Catal., B*, 2009, **90**, 595–602.

34 P. Goswami and J. N. Ganguli, Evaluating the potential of a new titania precursor for the synthesis of mesoporous Fe-doped titania with enhanced photocatalytic activity, *Mater. Res. Bull.*, 2012, **47**, 2077–2084.

35 A. K. Patra, A. Dutta and A. Bhaumik, Highly ordered mesoporous TiO_2–Fe_2O_3 mixed oxide synthesized by sol-gel pathway: an efficient and reusable heterogeneous catalyst for dehalogenation reaction, *ACS Appl. Mater. Interfaces*, 2012, **4**, 5022–5028.

36 T. Luttrell, S. Halpegamage, J. Tao, A. Kramer, E. Sutter and M. Batzill, Why is anatase a better photocatalyst than rutile? - Model studies on epitaxial TiO_2 films, *Sci. Rep.*, 2014, **4**, 4043.

37 J. Shi, G. Chen, G. Zeng, A. Chen, K. He, Z. Huang, L. Hu, J. Zeng, J. Wu and W. Liu, Hydrothermal synthesis of graphene wrapped Fe-doped TiO_2 nanospheres with high photocatalysis performance, *Ceram. Int.*, 2018, **44**, 7473–7480.

38 S. H. Othman, S. Abdul Rashid, T. I. Mohd Ghazi and N. Abdullah, Fe-Doped TiO2 Nanoparticles Produced via MOCVD: Synthesis, Characterization, and Photocatalytic Activity, *J. Nanomater.*, 2011, **2011**, 1–8.

39 W. Y. Teoh, R. Amal, L. Mädler and S. E. Pratsinis, Flame sprayed visible light-active Fe–TiO_2 for photomineralisation of oxalic acid, *Catal. Today*, 2007, **120**, 203–213.

40 P. Pongwan, B. Inceesungvorn, K. Wetchakun, S. Phanichphant and N. Wetchakun, Highly efficient visible-light-induced photocatalytic activity of Fe-doped TiO2 nanoparticles, *Eng. J.*, 2012, **16**, 143–151.

41 A. Bera, M. Mandal, M. Das, D. Chattopadhyay and S. Ghosh, An Experimental Design Study of Photocatalytic Activity of the Z-Scheme Silver Iodide/Tungstate Binary Nano Photocatalyst, *Environ. Sci. Pollut. Res.*, 2023, **30**, 35898–35910.

42 S. Sharma, R. Singh, R. P. Yadav, M. Kumar and P. Yadav, FeO-Clinoptilolite Nanoparticles: Brief Characterization and Its Photocatalytic Kinetics Towards 2,4-Dichloroaniline, *J. Hazard. Mater.*, 2022, **425**, 127883.

43 Y. Huang, X. Zhang, J. Li and L. Wang, Effects of Anion Vacancy in the Heterogeneous Photocatalytic Degradation, Part I: Focus on Sulfur, Nitrogen, Carbon, and Halogen Vacancies, *J. Mater. Sci.*, 2020, **55**, 10756–10789.

44 L. Zhang, X. Liu, X. Chen, Y. Sun and L. Zhang, A Comprehensive Review on the Boosted Effects of Anion Vacancy in the Heterogeneous Photocatalytic Degradation, Part II: Focus on Oxygen Vacancy, *J. Mater. Sci.*, 2021, **56**, 1345–1370.

45 L. Zhang, L. Zeng, Q. Luo, Y. Zhao, L. Zhang and Y. Sun, A Comprehensive Review on the Boosted Effects of Anion Vacancies in Photocatalytic Solar Water Splitting: Focus on g-C_3N_4 with Carbon and Nitrogen Vacancies, *J. Mater. Chem. A*, 2021, **9**, 9573–9603.

46 W. Zhou, L. Xie, J. Liu, Q. Huang and J. Zhang, A Comprehensive Review on the Boosted Effects of Anion Vacancy in the Photocatalytic Solar Water Splitting: Focus on Sulfur Vacancy, *J. Catal.*, 2020, **392**, 274–296.

47 M. Kruk and M. Jaroniec, Gas adsorption characterization of ordered organic-inorganic nanocomposite materials, *Chem. Mater.*, 2001, **13**, 3169–3183.

48 G. Limousin, J. P. Gaudet, L. Charlet, S. Szenknect, V. Barthès and M. Krimissa, Sorption isotherms: A review on physical bases, modeling and measurement, *Appl. Geochem.*, 2007, **22**, 249–275.

49 J. Z. Bloh, R. Dillert and D. W. Bahnemann, Zinc Oxide Photocatalysis: Influence of Iron and Titanium Doping and Origin of the Optimal Doping Ratio, *ChemCatChem*, 2013, **5**, 774–778.

50 L. Mandaric; M. Celic; R. Marcé and M. Petrovic, Introduction on Emerging Contaminants in Rivers and Their Environmental Risk, in *Emerging Contaminants in River Ecosystems: Occurrence and Effects Under Multiple Stress Conditions*, ed. M. Petrovic, S. Sabater, A. Elosegi and D. Barceló, Springer International Publishing, Cham, 2016, pp. 3–25.

51 R. Hossain, *Tunable Doping of Chromium in TiO_2 Nanocrystals Via Ion Diffusion*, Master's Thesis, University of South Dakota, Vermillion, SD, USA, 2019.

52 R. Hossain, M. A. Uddin and M. A. Khan, Mechanistic Understanding in Manipulating Energetics of TiO_2 for Photocatalysis, *J. Phys. Chem. C*, 2023, **127**, 10897–10912.

53 R. Hossain and A. Apblett, Cr^{3+}-Doped Anatase-Phase TiO_2 Nanocrystals with (101) and (004) Dominant Facets: Synthesis and Characterization, *Catalysts*, 2025, **15**, 33.

54 E. Ahmadpour, A. Naseri, M. Abdollahi and S. Ghasemi, A Comprehensive Study on the Mechanism Pathways and Scavenging Agents in the Photocatalytic Activity of $BiVO_4$/WO_3 Nano-Composite, *J. Environ. Chem. Eng.*, 2024, **12**, 110125.

55 R. Rahimi, A. Naseri and M. Ghaemi, A Z-Scheme Cobalt(II) Oxide–Silver Tungstate Nano Photocatalyst: Experimental Design and Mechanism Study for the Degradation of Methylene Blue, *J. Mol. Struct.*, 2024, **1292**, 136956.

56 P. Gholami, B. Yazdani and M. M. Amini, A Visible Light Driven AgBr/g-C_3N_4 Photocatalyst Composite in Methyl

Orange Photodegradation: Focus on Photoluminescence, Mole Ratio, Synthesis Method of g-C_3N_4 and Scavengers, *Colloids Surf., A*, 2023, **660**, 130959.

57 M. Abdollahi and A. Naseri, A Quadripartite Cu_2O–CdS–$BiVO_4$–WO_3 Visible-Light Driven Photocatalyst Containing Three Cascade Z-Scheme Systems: Focus on Conditions' Optimization, Scavenging Agents and the Mechanism Pathway towards Sulfasalazine, *Iran. J. Catal.*, 2025, **15**, 186–202.

58 Z. Heidari, S. Ghasemi and D. Salari, A Magnetically Separable Clinoptilolite Supported CdS–PbS Photocatalyst: Characterization and Photocatalytic Activity toward Cefotaxime, *Mater. Chem. Phys.*, 2024, **305**, 128100.

59 A. Nezamzadeh-Ejhieh and Z. Banan, Kinetic Investigation of Photocatalytic Degradation of Dimethyldisulfide by Zeolite A Containing Nano CdS, *Iran. J. Catal.*, 2012, **2**, 79–83.

60 S. Mohan, V. Sivasankar, S. Suresh, S. Rajendran and K. Natarajan, Photocatalytic Degradation of Metronidazole Using Co-Precipitation Synthesized $Zn(\text{II})/Ni(\text{II})$ Ferrite Nanoparticles, *J. Environ. Chem. Eng.*, 2018, **6**, 3575–3583.

61 P. Kumar, S. K. Sahu, K.-H. Kim, R. J. Brown and V. K. Gupta, Photocatalytic Degradation of Sulfasalazine Using Cu_2O/CdS Nanoparticles under Visible Light Irradiation, *Environ. Sci. Technol.*, 2016, **50**, 8022–8030.